Eun-Hwa Kim[1] and Jay R. Johnson[2]

1 Princeton Plasma Physics Laboratory, Princeton University, Princeton, NJ

2 Andrews University, Berrien Springs, MI

Corresponding author: Eun-Hwa Kim (ehkim@pppl.gov)

Key Points:

- Wave mode coupling of solar wind fluctuation to magnetospheric fluctuation is examined using an advanced 2D-full wave simulation code, Petra-M.
- Compressional waves from a high latitude source can propagate into the inner magnetosphere and reach the ground near the cusp region.
- Linearly polarized EMIC waves can externally be driven by solar wind via mode conversion at the Alfven and ion-ion hybrid resonances.

Abstract

We examine the wave coupling efficiency of solar wind to magnetospheric fluctuations in the ULF frequency range using an advanced full-wave simulation code, Petra-M. Earth's magnetic field is tilted to the ecliptic plane; thus, compressional wave sources can be incident over a wide range of magnetic latitudes. When compressional waves are incident at a low latitude, very little wave power can reach the inner magnetosphere. On the other hand, waves incident from a high latitude source can propagate efficiently into the inner magnetosphere and reach the ground near the cusp region. The mode-conversion and polarization reversal at the crossover plays a critical role in compressional wave propagation. The mode-converted linearly polarized electromagnetic ion cyclotron waves also occur at the Alfvén and ion-ion hybrid resonances. Therefore, the results suggest that solar wind compression can drive the linearly polarized EMIC waves, and the wave occurrence can have seasonal and diurnal dependence.

Plain Language Summary

Earth's magnetic field is tilted to the ecliptic plane, and this angle has seasonal and diurnal variations. Thus, the magnetic latitude of compressional wave source (assuming wave propagation in sun-earth direction) can be incident over a wide range of magnetic latitudes. When the solar wind fluctuations incident along the ecliptic plane, the wave energy can be transferred to the ultra-low frequency magnetospheric fluctuations. In this paper, we examine the effect of the tilt of Earth's magnetic field on this mode coupling using an advanced full-wave simulation code, Petra-M. There are striking differences in wave coupling along the magnetic latitude of the source wave. When solar wind fluctuations are incident at a low latitude, they are almost totally reflected. On the other hand, waves from a high latitude source can propagate efficiently into the inner magnetosphere and reach the ground near the higher magnetic latitude in the polar region. In this case, compressional fluctuations in the solar wind can be converted to the linearly polarized, field-aligned propagating waves in the inner

and outer magnetosphere. Therefore, the results suggest that solar wind compression can drive the linearly polarized EMIC waves, and the wave occurrence can have seasonal and diurnal dependence.

1 Introduction

Ultra-low frequency electromagnetic ion cyclotron (EMIC) waves in the Pc 1-2 frequency range are a prominent feature of the magnetosphere-ionosphere (e.g., J. H. Lee et al., 2021; Usanova, 2021; Noh et al., 2022; Engebretson et al., 2021). Early theoretical work suggested that EMIC waves are transverse left-handed polarized waves generated near the magnetic equator by anisotropic protons (e.g., Cornwall, 1965); however, various polarizations, such as right- (RHP), left-handed (LHP), and linear polarization, are also reported (e.g., Anderson et al., 1992; Min et al., 2012; Saikin et al., 2015; Allen et al., 2015). The occurrences of linear polarization waves in the outer magnetosphere are comparable to the LHP waves (Min et al., 2012; Allen et al., 2015) and even dominant in the inner magnetosphere (Saikin et al., 2015; Wang et al., 2017; Jun et al., 2019, 2021).

While LHP EMIC waves are expected to result from linear growth of an anisotropy-driven instability, the origin of linear polarization is not fully understood. The dispersion relation of EMIC waves in a multi-ion plasma indicates that any branch of the wave mode should be predominantly LHP or RHP, except for a few exceptions near the crossover frequency (Smith & Brice, 1964; Fraser, 1985) or at oblique propagation near the multi-ion hybrid resonances (Buchsbaum, 1960).

While polarization reversal at the crossover frequency was clearly seen in the spectrograms of proton whistlers (Gurnett et al., 1965; Kim & Lee, 2005) and has been associated with linear polarization of some observed EMIC waves (Sakaguchi et al., 2013), these studies were more focused on wave propagation and did not consider the possibility of mode conversion between RHP and LHP wave modes near this frequency. Johnson et al. (1995) and Johnson and Cheng (1999) found that significant wave energy could be transferred between two different wave modes at the crossover, and 2D-full simulations later showed that the crossover frequency has a critical role for EMIC wave propagation to the ground (Kim & Johnson 2016).

External compressions are one of the possible sources of waves in the Pc frequency range in the magnetosphere (Anderson & Hamilton, 1993; Keika et al., 2013; Gamayunov & Engebretson, 2021), and the EMIC waves can be externally generated via mode conversion at the ion-ion hybrid (IIH) resonance (Klimushkin et al., 2006; D.-H. Lee et al., 2008; Mikhailova et al., 2019) in analogy with the standard field-line resonance (e.g., D.-H. Lee & Lysak, 1989). This mode conversion occurs as a compressional wave propagates radially inward into an increasing magnetic field region (or into a heavy-ion density gradient) and encounters the IIH resonance. Up to 100% of the incoming wave energy at this location can be converted to a field-aligned IIH wave mode (D.-H. Lee et al., 2008; Kim, Johnson, & Lee, 2019), although for typical heavy ion concentrations

the conversion is far less efficient. A 1D full wave calculation also showed that mode conversion at the IIH resonance occurs over a narrow frequency range near but not at the crossover (Kim, Johnson, Kim, & Lee, 2015).

The IIH resonance has been examined using a 2D full-wave simulation (FW2D) code at Mercury and Earth. Strong mode conversion occurs at Mercury's magnetosphere in a wide range of L-shell (Kim, Johnson, Valeo, & Phillips, 2015); however, mode-converted IIH wave power at Earth was weaker than at Mercury (Kim et al., 2017). These differences can stem from the physical parameters (such as magnetic field strength or field line length) or simulation conditions (such as initial wave source). For example, both full-wave simulations assumed a low magnetic latitude compressional wave source near the magnetic equator, and the mode conversion efficiency is very similar to that predicted by the 1D model. This assumption is relevant to Mercury because Mercury's magnetic equator is almost parallel to the ecliptic plane (Klaasen, 1976; Philpott et al., 2014). However, Earth's magnetic field is tilted with respect to the Sun. Seasonal effects, due to the inclination of the Earth's rotation axis to the ecliptic, contribute 23.5° of the annual tilt angle variation, with the remaining 10.5° arising from the offset of the geomagnetic dipole to the rotation axis (Hapgood, 1992). Thus, the angle between the ecliptic plane and dipole axis can up to 34° at Earth at solstice, which can significantly affect the latitude of the external wave source. For this reason, it is needed to consider a compressional wave source at the higher magnetic latitude, when the magnetic tilt effect is maximized.

In this paper, we expand on the previous 2D full-wave simulation by considering the magnetic tilt effects on externally driven EMIC waves, which effectively shifts the source to higher geomagnetic latitude. We use an advanced full-wave simulation code, Petra-M (Physics Equation Translator for MFEM) (Shiraiwa et al., 2017), developed for radio frequency wave propagation in fusion devices. By adopting the Earth's dipole geometry in the Petra-M code, we launch compressional waves at different magnetic latitudes to demonstrate the magnetic tilt effects.

This paper is organized as follows. In section 2, we briefly describe wave dispersion relations in multi-ion plasma. We discuss the wave group velocity direction and polarization of each wave mode. Section 3 provides a brief introduction of the Petra-M code and the simulations. Wave solutions showing the electric field, Poynting flux, and ellipticity are presented for external wave sources at low and high magnetic latitude. The last section includes the discussion and summary.

2 Wave dispersion relation in multi-ion plasma

Plasma waves in the ion cyclotron frequency range propagating parallel to $\mathbf{B}_0$ are RHP or LHP in the dispersion relation. Including heavier ions introduces a crossover frequency ($_{\mathrm{cr}}$), where the RHP and LHP branches cross each other, and a cutoff frequency ($_{\mathrm{Lcut}}$) for the LHP branch, and a Buchsbaum resonance frequency ($_{\mathrm{bb}}$), between two ion cyclotron frequencies (See Section 2 in Kim,

Johnson, & Lee, 2019). When waves propagate obliquely, RHP and LHP waves are coupled at $_{cr}$. Figure 1 illustrates (a) a wave dispersion relation for 30° wave normal angle and (b) the refractive surface in an H^+-He^+ plasma. The color bar represents a wave ellipticity, and ± signs are RHP (red color) and LHP (blue), respectively.

In the dispersion relation in Figure 1(a), we refer to class I, He^+ cyclotron wave branch, class II, connected to the magnetosonic wave branch, and class III connected to the H^+ cyclotron waves (Rauch & Roux, 1982). At $= _{cr}$, polarization reversal of class II (between A and B in Figure 1(a)) and class III (between C and D) waves occurs, and waves have linear polarization at $_{cr}$. Both class I and III waves can also have linear polarization for $= _{cO}$, where $_{cO}$ is an oxygen gyrofrequency.

Mode conversion between class II and class III branches also occurs at $_{cr}$ (Johnson et al., 1989, 1995; Kim & Johnson, 2016). When class III LHP waves (class III_{LH}, marked as C in Figure 1(a)) close to $_{cr}$, the wave energy can be transferred to the class II RHP (class II_{RH}, marked as A) and LHP (class II_{LH}, marked as B) waves. Reversed mode conversion from class II_{RH} (marked as A) to class III_{LH} (marked as C) and class III_{RH} (marked as D) waves also occur. This coupling is very strong for small angle of propagation and decreases as the fourth power of the angle with increasing angle.

We also plot the refractive surface of class III waves as shown in Figure 1(b) to examine wave group velocity direction. Here, we only present the class III wave mode because the refractive surface of class III is the most complicated among the three classes and the most important class for EMIC wave generation and propagation. In this figure, we can determine the group velocity (V_g), which is perpendicular to the refractive index surface (Rauch & Roux, 1982). For $> _{cr}$ in the top panel of Figure 1(b), V_g is almost parallel to $\mathbf{B}_0$ even for n n, where $n_{()}$ is the refractive index perpendicular (parallel) to $\mathbf{B}_0$; thus, these waves are almost guided along $\mathbf{B}_0$. For $= _{cr}$, the waves have linear polarization and perfectly guided as expected. For $_{bb} < < _{cr}$ in the middle panel, waves are still guided but they are RHP. As wave frequency decreases and becomes closer to $_{bb}$, the refractive surface becomes curved, and it is closed for $< _{bb}$ in the bottom panel. These waves are RHP and unguided. The refractive surface of class I (not shown here) is similar to the upper panel of class III; they are guided LHP waves, and class II waves (not shown here) are unguided LHP or RHP waves.

For $n \gg n$, the dispersion surface of class III of $> _{bb}$ is parallel to $\mathbf{B}_0$, which represents the ion-ion hybrid (IIH) resonance. The dispersion relation of the magnetosonic wave branch can be written as

$$n_\perp^2 = \frac{(R-n_\parallel^2)(L-n_\parallel^2)}{(S-n_\parallel^2)} \quad (1)$$

And the IIH resonance occurs where $n \to \infty$ at $n^2 \quad S$. The mode converted wave propagates along the magnetic field line with dispersion relation of $n^2 \quad S$

and has large wave normal angle (e.g., Kim, Johnson & Lee, 2019)

3 Full-wave Simulations

An electromagnetic simulation code, Petra-M, for modeling radio frequency (RF) plasma wave propagation in the fusion device is developed (Shiraiwa et al., 2017). This code uses the MFEM (modular finite element method) library (https://mfem.org/) developed by Lawrence Livermore National Laboratory and includes newly developed Python wrapper for MFEM and a RF wave physics module. This code uses the same numerical technique of the finite element method (FEM) with the FW2D code (Kim, Johnson, Valeo, & Philips, 2015) but provides higher order accurate solutions. The code computes the wave power, Poynting flux, and wave absorption when waves are launched from a source location and successfully used for the several tokamak machines (e.g., Shiraiwa et al., 2017, Bertelli et al., 2020)

One advantage of using the FEM is that the local basis functions can be readily adapted to boundary shapes and background parameters, such as multiple particle densities, magnetic field configuration, and strength, and provides higher resolution in regions where solutions exhibit singular behavior and mode conversion occurs. For such reasons, various magnetic field topologies (i.e., planetary magnetospheres and tokamaks) have been adopted in the FW2D code (Kim et al., 2016, 2017; Kim, Bertelli, Ono et al., 2019).

In this paper, we utilized a dipole magnetic field configuration in the Petra-M code. The linear and cold plasma wave equation

$$\nabla \times (\nabla \times \mathbf{E}) - \frac{\omega^2}{c^2} \bullet \mathbf{E} = i\omega\mu_0 \mathbf{J}_{\text{ext}} \quad (2)$$

is solved in the RF module of Petra-M simulation code. Here is an angular frequency, $\mathbf{E}$ is the perturbed electric field, $\mathbf{J}_{\text{ext}}$ is the (localized) external current source launching the waves within our model, is the dielectric tensor, c is a light speed, and $_0$ is the vacuum permeability. We perform 2D simulations in the cylindrical coordinate ($\mathbf{r}$, , and $\boldsymbol{z}$), and the output solutions are transferred to coordinates aligned along and across the $\mathbf{B}_0$ direction (, , and $\mathbf{b}$), where $\mathbf{b} = \mathbf{B}_0/\mathbf{B}_0$ is the unit vector along the magnetic field line, is the azimuthal direction, and is normal to the field line pointing outward ($=$ $\times\mathbf{b}$). For simplicity, we assume an azimuthal wave number $m = 0$. We adopt a dipole magnetic field and the empirical electron density model (Denton et al., 2006),

$$N_e = 1390 \left(\frac{3}{L}\right)^{4.83} \left(\frac{L}{R/R_E}\right)^{0.8}, \quad (3)$$

where R is a geocentric distance and R_E is Earth's radii. We choose a typical heavy ion density concentration ratio, 10% He^+ and 5% O^+ and the wave frequency of $f = 0.1$Hz, which satisfies $_{\text{cO}} <$ $<$ $_{\text{cHe}}$ at the source location. We adopt a simulation domain $0.1 < x/R_E < 11.5$ and $-6 < z/R_E < 7.5$ to consider the inner and outer magnetosphere. In order to simulate outgoing boundary conditions, we implement a strong absorption layer near the boundary. This layer effectively absorbs all waves leaving the simulation domain without reflection.

A weak collision frequency (10^{-4}) is also applied throughout simulation domain to eliminate singular points at the ion cyclotron resonances. As in the case of 1D full wave calculations (Johnson & Cheng, 1999), the solutions are not sensitive this weak collision frequency as long as it remains well below the wave frequency. Two incoming compressional wave sources are considered at magnetic equator and higher magnetic latitude at $R = 10R_E$, and source sizes along the normal and tangential component of the geocentric direction are 0.1 and $0.5R_E$, respectively.

3.1 Low magnetic latitude compressional wave source (No magnetic tilt effect)

We first consider a low latitude compressional wave source. Figure 2 shows the wave solutions of the fluctuating electric ($\boldsymbol{E}$) fields, the Poynting flux ($\boldsymbol{S}$), and ellipticity in the magnetosphere. Here $\boldsymbol{E}$ and $\boldsymbol{S}$ are normalized to the maximum amplitude in the whole simulation domain (E_{max} and S_{max}) or the total amplitude S_{tot} in each local mesh. In this case, the Earth's magnetic equator is assumed to be along the ecliptic plane; thus, we launch magnetosonic branch class II waves in E (marked as A in Figure 2) at the magnetic equator, $L = 10$ and MLAT=0° with a wavevector aligned with the equator. This wavevector is imposed by the shape of the current source imposed in the simulation domain.

Waves radiate both inward and outward away from the wave source. The waves propagating toward the outer magnetosphere are totally absorbed near the outer boundary without reflection, so these outgoing waves do not affect the wave solutions in the inner magnetosphere. On the other hand, waves propagating toward Earth reach the crossover location ($l_{\rm cr}$), where $= {}_{\rm cr}$ (marked as B), and the waves have linear polarization as shown in Figure 2(f) as predicted in the dispersion relation in Figure 1. The waves propagate as LHP wave beyond $l_{\rm cr}$ and reflect at the cutoff location where $= {}_{\rm Lcut}$ (marked as C) and propagate outward toward the outer magnetosphere. The field-aligned Poynting flux is very weak as shown in Figure 2(d) and most wave energy flows perpendicular to $\mathbf{B}_0$. Here, no clear evidence of the IIH resonance was found, like the previous simulation (Kim et al., 2017).

We also found waves propagating along the field line (marked as D) in Figure 2(b). These waves are mode-converted class $\rm III_{RH}$ waves at $l_{\rm cr}$ and propagate to the higher magnetic latitude. The class $\rm III_{RH}$ waves become unguided below the $l_{\rm bb}$ where $= {}_{\rm bb}$ and refracted toward the magnetic equator in the inner magnetosphere. Another mode conversion from these waves to the linearly polarized waves (marked as E in Figure 2(a)) occurs at the Alfvén resonance in the inner magnetosphere. The mode converted waves are field-aligned propagating waves oscillating in E (and B, not shown here) and mixed field-aligned Poynting flux because of reflection at Earth's surface, which is the same as the field line resonance. However, the field line resonance wave power is negligible in this case.

It should be noted that the efficiency of this mode conversion process decreases as the concentration of heavy ions (particularly $\rm He^+$) increases [D.-H. Lee et al.,

2008], and it is expected that very little wave power reaches the inner magnetosphere unless the heavy ion concentrations drop below one percent, which is typically well below observed concentration levels.

3.2 High magnetic latitude compressional wave source (Magnetic tilt effect)

We next examine wave propagation when the compressional wave is launched at a high magnetic latitude. In this case, the waves are launched by imposing E at $L = 14.9$ and MLAT$= 34°$ (marked as A in Figure 3). In contrast to the low latitude wave source shown in Figure 2, these compressional waves have linear polarization consistent with the local dispersion relation because the source location is close to $l_{\rm cr}$.

Wave propagation in Figure 3 is dramatically changed from Figure 2. The incoming class II $_{\rm RH}$ compressional waves propagate along the ecliptic plane and become class $\rm II_{LH}$ waves at $l_{\rm cr}$. These polarization reversed waves are reflected at $l_{\rm Lcut}$ and propagate towards the outer magnetosphere (marked as B). Mode conversion from class II to class III also occurs at $l_{\rm cr}$. The mode-converted class $\rm III_{RH}$ waves can propagate across $l_{\rm Lcut}$ and are quasi-guided by $\mathbf{B}_0$ between $l_{\rm cr}$ and $l_{\rm bb}$ as described in Figure 1 (marked as C in Figure 3). The waves are refracted beyond $l_{\rm bb}$ and propagate as RHP waves to the lower magnetic latitude (marked as D). These waves also can partially propagate in the field-aligned direction and are coupled to field-aligned propagating Alfvén waves at $<$ $_{\rm cO}$ (marked as E). In the cusp area, the Alfvén speed becomes much higher than at the magnetic equator, thus the wavelength in Figure 3(a) is much longer than other waves.

As shown in Figure 3, both class $\rm II_{LH}$ and class $\rm III_{RH}$ are unguided and propagate toward the magnetic equator. Unlike Figure 2, strong mode conversion from these waves to the IIH resonant waves (marked as F) occurs in the outer magnetosphere. In this case, the wavelength parallel to $\mathbf{B}_0$ is satisfies the resonance condition $n^2 = S$ over a range of L-shells, and linearly polarized EMIC waves are generated via mode conversion in $7.5 < L < 8.5$. The mode converted IIH waves propagate with dispersion relation of $n^2 = S$, thus they have cutoff condition at the Buchsbaum location ($S = 0$, $l_{\rm bb}$), and a resonance condition at the ion cyclotron frequency ($S \to \infty$, $l_{\rm cO}$), and a stop gap between $l_{\rm bb}$ and $l_{\rm cO}$. Depending on local heavy ion density and azimuthal wavenumber, the IIH waves can tunnel through this stopgap; however, for the given condition, the waves cannot penetrate the stopgap and are localized near the lower MLAT in between the northern and southern cutoff location. Although the compressional waves propagate downward (thus, mostly anti-parallel to $\mathbf{B}_0$), the Poynting flux of the IIH waves includes both parallel and anti-parallel directions due to wave reflection at $l_{\rm bb}$. The mode-converted waves have a longer wavelength along the field line than across the field line as expected for the resonance conditions with $n \gg n$.

Since class $\rm III_{RH}$ waves below $_{\rm bb}$ are unguided, these waves can also propagate into the inner magnetosphere. These waves can be trapped in the inner mag-

netosphere and reach ionospheric altitudes, as shown in Figure 3(b). For the given condition, waves in the inner magnetosphere $L < 6.6$ are always below f_{cO}, and these linearly polarized waves correspond to field line resonances, are seen in these lower L-shell (marked as G). Unlike the typical field line resonance in the Pc 5 frequency range, these wave frequencies are still comparable to the ion cyclotron frequency, and the field-aligned wavelength is much shorter than the Pc 5 waves.

In contrast to the case of low magnetic field latitude incidence, the efficiency of mode coupling to the inner magnetosphere increases as the concentration of heavy ions increases. This behavior makes it possible for storm-time feedback where waves reaching the ionosphere could energize heavy ions leading to increased wave coupling.

4 Discussion and Summary

This paper examines compressional wave propagation when the waves are incident at low and high magnetic latitude and demonstrates how the magnetic tilt angle can significantly affect wave propagation. Although low latitude compressional waves propagate toward Earth, they almost totally reflect at a cutoff and very little wave power can reach the IIH resonance, consistent with the previous 2D full-wave simulation (Kim et al., 2017). On the other hand, when waves are incident from a source at higher magnetic latitude, the wave energy can effectively reach the ground along the field line and be trapped in the inner and outer magnetosphere via mode conversion to the Alfvén and IIH resonances. This work suggests with that solar wind compressions can drive EMIC waves externally when the dipole angle is tilted toward or away from the Sun-Earth direction.

The results of the higher magnetic latitude source. First, the incoming waves can directly reach the ground at a higher magnetic latitude. In Figure 3, incoming class $\mathrm{II}_{\mathrm{RH}}$ waves are converted to the class $\mathrm{III}_{\mathrm{RH}}$ waves at the crossover frequency and propagate toward Earth. These waves are coupled with the Alfvén waves near Earth and finally reach the foot point of the wave source near the cusp region. The magnetic tilt angle would maximize local summer and minimize near the equinox. The dipole angle is tilted toward the Sun-Earth direction during the local summer, and thus waves easily reach the same hemisphere as the source location. Therefore, our simulations support the detected EMIC wave occurrence at a near-cusp station in Antarctica, showing maximum occurrence in the local summer (Regi et al., 2017).

Second, we show that strong IIH resonance occurs in the outer magnetosphere. Once the compressional waves satisfy the IIH or Alfvén resonance conditions, mode conversion can occur. This resonance occurs wide range of L-shell, which is unexpected from the 1D simulations. As shown in Figure 3, incoming waves spread a wide range of L-shell; thus, these waves can match the IIH resonance condition in various magnetic latitudes and L-shells. Once the mode conversion occurs, the wave energy is strongly guided by $\mathbf{B}_0$. This result is consistent with

wave observation showing linear polarized EMIC waves detected over a broad range of L-shell in the inner magnetosphere (e.g., Chaston et al., 2015).

Third, we show that the mode conversion at the crossover is critical to EMIC wave propagation from the outer to inner magnetosphere (Johnson et al., 1995). Previous 2D wave simulations also presented the RHP wave propagation into the inner magnetosphere (Kim & Johnson, 2016; Pakhotin et al., 2022), however, the previous simulations and this study launched different wave modes (class $\mathrm{III_{LH}}$ and class $\mathrm{II_{RH}}$). While the RHP waves in the inner magnetosphere in the previous simulations are due to the polarization reversal, the RHP waves in Figure 3 are due to mode-conversion at l_{cr}. This result also emphasizes the role of crossover frequency on EMIC wave propagation. The class $\mathrm{III_{RHP}}$ waves can reach the inner magnetosphere independent of the polarization of the source waves.

However, our simulation does not show direct evidence of mode conversion from class $\mathrm{II_{RH}}$ (marked as A in Figure 1(b)) to class $\mathrm{III_{LH}}$ (marked as C in Figure 1(b)) waves, while Kim & Johnson (2016) showed the reversal mode conversion process. The absence of mode conversion results because the efficiency from class $\mathrm{II_{RH}}$ to the class $\mathrm{III_{LH}}$ waves is much lower than to the class $\mathrm{III_{RH}}$ waves (Johnson et al., 1995). The same mode-conversion process (from class $\mathrm{II_{RH}}$ to class $\mathrm{II_{LH}}$) has been suggested to examine the generation of ELF waves (f 60Hz) (Horne & Miyoshi, 2016), but they ignore the mode conversion from class $\mathrm{II_{RHP}}$ to class $\mathrm{III_{RHP}}$ modes, which has higher mode conversion efficiency (Johnson et al., 1995).

Fourth, EMIC waves can be detected in a wide range of L-shell at the satellite and ground-based magnetometers, and these waves are all from a single wave source. In addition to the EMIC waves reaching the higher magnetic latitude and IIH resonance in the outer magnetosphere, we also found the secondary mode conversion to the field line resonance in the inner magnetosphere from the class $\mathrm{III_{RH}}$ waves (Pakhotin et al., 2022). Thus, when the compressional source is off the equator at L=14.9, linearly polarized EMIC waves can be detected at L 7 on the ground and satellites, near 7.5$<L<$8.5 at the low magnetic latitude magnetosphere, and at the foot point of the source location, respectively.

We clearly demonstrate the magnetic tilt effects on EMIC wave generation and propagation in the inner and outer magnetosphere. However, there are several limitations to this paper. As seen in the figures, the compressional wave propagation into the inner magnetosphere is one of the key processes to consider in the generation of linear polarization waves, and compressional wave propagation is strongly affected by the background density profile. In this paper, we adopted an empirical density model (Denton et al., 2006) which is relevant to the outer magnetosphere. We also do not consider the plasmapause effect. The low-frequency compressional wave energy can be trapped in the plasmasphere, and virtual resonance also can occur (D.-H. Lee & Takahashi, 2006). Thus, realistic global density profiles, such as GCPM model (Gallagher et al., 2000), should be considered for further study (Kim et al., 2017, Pakhotin et al., 2022).

We assume a constant heavy ion density profile throughout the simulation domain and do not consider the azimuthal wave propagation effect ($m = 0$). When He^+ ion density increases, the cutoff condition for the field-aligned waves shifts toward the outer magnetosphere and lower magnetic latitude. Thus, the wave stopgap between cutoff and resonance locations becomes wider, and waves cannot penetrate the stopgap. As a result, we found that even a 5% O^+ density prevents the IIH wave propagation to the ground. For a constant m, the azimuthal wavevector $k \quad m/r$ increases when waves propagate close to Earth. When k increases, the evanescent region between cut-off and resonance increases; thus, resonant absorption is expected to decrease (Kim et al., 2011). On the other hand, unlike IIH resonance, resonant absorption at the Alfvén resonance is expected to increase for $m \quad 0$.

In addition, we adopt a dipole magnetic field topology, even though we consider the dayside outer magnetosphere. The magnetic field on the dayside is compressed, and the different magnetic field shapes will affect the dayside compressional wave propagation. The magnetic tilt angle with IMF incident angle strongly affects the geomagnetic field line configurations (Park et al., 2010; Eggington et al., 2020), and north-south and east-west asymmetries of the magnetic field occur. Therefore, wave simulations in a realistic magnetic field topology should be followed in the future.

Data Availability Statement

The raw data supporting the conclusions of this article will be made available by the authors, without undue reservation. Digital data can be found in the Data Space of Princeton University (https://dataspace.princeton.edu/handle/88435/dsp01pz50gz45g).

Acknowledgment

Author Kim thanks to Dr. Shiraiwa for his technical support and to Profs. M. Engebretson and K.-H. Kim for the valuable discussion. This material is based upon work supported by the U.S. Department of Energy, Office of Science, Office of Fusion Energy Sciences under contract DE-AC02-09CH11466. Work at Princeton University is under National Science Foundation (NSF) Grant AGS1602855 and National Aeronautics and Space Administration (NASA) Grants 80HQTR18T0066, 80HQTR19T0076, and NNX17AI50G. Work at Andrews University is supported by NASA grants NNX16AQ87G, 80NSSC19K0270, 80NSSC19K0843, 80NSSC18K0835, 80NSSC20K0355, NNX17AI50G, 80HQTR18T0066, 80NSSC20K0704, 80NSSC18K1578, 80NSSC22K0515, and NSF grants AGS1832207, AGS1602855, and AGS2131013.

References

Allen, R. C., Zhang, J.-C., Kistler, L. M., Spence, H. E., Lin, R.-L., Klecker, B., . . . Jordanova, V. K. (2015). A statistical study of EMIC waves observed by Cluster: 1. Wave properties. *Journal of Geophysical Research Space Phys.*, 120, doi:10.1002/2015JA021333.329

Anderson, B. J., Erlandson, R. E., & Zanetti, L. J. (1992). A statistical study of Pc 1-2 magnetic pulsations in the equatorial magnetosphere 2. Wave properties. *Journal of Geophysical Research*, 97 (A3), 3089–3101.

Anderson, B. J., & Hamilton, D. J. (1993). Electromagnetic ion cyclotron waves stimulated by modest magnetospheric compressions. *Journal of Geophysical Research*, 98, 11369.

Bertelli, N., S. Shiraiwa, G. J. Kramer, X. Yang, T. DeHaas, C. Lau, B. V. Compernolle, E.-H. Kim, and J. C. Wright (2020), 3D full wave fast wave modeling with realistic antenna geometry and SOL plasma, AIP Conference Proceedings, 2254(1), 030,001, doi:10.1063/5.0013580.

Buchsbaum, S. J. (1960). Ion resonance in a multicomponent plasma. *Physical Review Letters*, 5, 495–497.

Chaston, C. C., J. W. Bonnell, C. A. Kletzing,G. B. Hospodarsky, J. R. Wygant, and C. W.Smith (2015), Broadband low-frequency electromagnetic waves in the inner magnetosphere, *J. Geophys. Res. SpacePhysics*,120, 8603–8615, doi:10.1002/2015JA021690.

Cornwall, J. M. (1965). Cyclotron instabilities and electromagnetic emission in the ultra low frequency and very low frequency ranges. *Journal of Geophysical Research*, 70, 61, doi:10.1029/JZ070i001p00061.346

Denton, R. E., Takahashi, K., Galkin, I. A., Nsumei, P. A., Huang, X., Reinisch, B. W., . . . Hughes, W. J. (2006). Distribution of density along magnetospheric field lines. *Journal of Geophysical Research*, 111 (A10), 04213.

Eggington, J. W. B., Eastwood, J. P., Mejnertsen, L., Desai, R. T., & Chittenden, J. P. (2020). Dipole tilt effect on magnetopause reconnection and the steady-state magnetosphere-ionosphere system: Global MHD simulations. *Journal of Geophysical Research: Space Physics*, 125 (7), doi: https://doi.org/10.1029/2019JA027510360

Engebretson, M. J., L. Y. Ahmed, V. A. Pilipenko, E. S. Steinmetz, M. B. Moldwin, M. G. Connors, D. H. Boteler, J. M. Weygand, S. Coyle, S. Ohtani, J. Gjerloev, and C. T. Russell (2021a), Superposed epoch analysis of nighttime magnetic perturbation events observed in arctic Canada, *Journal of Geophysical Research: Space Physics*, 126(9), e2021JA029,465, doi: https://doi.org/10.1029/2021JA029465, e2021JA029465 2021JA029465.

Fraser, B. J. (1985). Observations of ion cyclotron waves near synchronous orbit and on the ground. *Space Science Reviews*, 42, 357– 374.

Gallagher, D. L., Craven, P. D., & Comfort, R. H. (2000). Global core plasma model. *Journal of Geophysical Research*, 105, 18,819.

Gamayunov, K. V., & Engebretson, M. J. (2021). Low frequency ULF waves in the Earth's inner magnetosphere: Statistics during coronal mass ejections and

seeding of EMIC waves. *Journal of Geophysical Research: Space Physics*, 126, e2021JA029247. https://doi.org/10.1029/2021JA029247

Gurnett, D. A., Shawhan, S. D., Brice, N. M., & Smith, R. L. (1965). Ion Cyclotron Whistlers. *Journal of Geophysical Research*, 70, 1665.

Hapgood, M. (1992). Space physics coordinate transformations: A user guide. *Planetary and Space Science*, 40 (5), 711–717. doi:https://doi.org/10.1016/0032-0633(92)90012-D

Horne, R. B., & Miyoshi, Y. (2016). Propagation and linear mode conversion of magnetosonic and electromagnetic ion cyclotron waves in the radiation belts. *Geophysical Research Letters*, 43 (19), 10,034-10,039. doi: https://doi.org/10.1002/2016GL070216

Johnson, J. R., Chang, T., & Crew, G. B. (1995). A study of mode conversion in an oxygen-hydrogen plasma. *Physics of Plasmas*, 2, 1274–1284, https://doi.org/10.1063/1.871339.

Johnson, J. R., Chang, T., Crew, G. B., & Andre, M. (1989). Equatorially generated ULF waves as a source for the turbulence associated with ion conics. *Geophysical Research Letters*, 16, 1469–1472, doi:10.1029/GL016i012p01469.

Johnson, J. R., & Cheng, C. Z. (1999). Can ion cyclotron waves propagate to the ground? *Geophysical Research Letters*, 26, 671–674, https://doi.org/10.1029/1999GL900074.

Jun, C.-W., Miyoshi, Y., Kurita, S., Yue, C., Bortnik, J., Lyons, L., . . . Shinohara, I. (2021). The characteristics of EMIC waves in the magnetosphere based on the Van Allen Probes and Arase observations. *Journal of Geophysical Research: Space Physics*, 126 (6), e2020JA029001. doi: https://doi.org/10.1029/2020JA029001

Jun, C.-W., Yue, C., Bortnik, J., Lyons, L. R., Nishimura, Y., & Kletzing, C. (2019). EMIC wave properties associated with and without injections in the inner magnetosphere. *Journal of Geophysical Research: Space Physics*, 124 (3), 2029–2045. doi:https://doi.org/10.1029/2018JA026279

Keika, K., Takahashi, K., Ukhorskiy, A., & Miyoshi, Y. (2013). Global characteristics of electromagnetic ion cyclotron waves: Occurrence rate and its storm dependence. *Journal of Geophysical Research*, 118, 4135, doi: 10.1002/jgra.50385.

Kim, E.-H., Bertelli, N., Johnson, J. R., Valeo, E., & Hosea, J. (2017). 2D full-wave simulation of waves in space and tokamak plasmas. *European physical journal web of conference*, 157, 02005, doi:10.1051/epjconf/201715702005.

Kim, E.-H., Bertelli, N., Ono, M., Valeo, E. J., Hosea, J. C., and Perkins, R. J. (2019), Effect of wall boundary on the scrape-off layer losses of high harmonic fast wave in NSTX and NSTX-U, Physics of Plasmas, 26(6), 062,501, doi:10.1063/1.5091579.

Kim, E.-H., & Johnson, J. R. (2016). Full-wave modeling of EMIC waves near the He^+ gyrofrequency. *Geophysical Research Letters*, doi:10.1002/2015GL066978.

Kim, E.-H., Johnson, J. R., Kim, H., & Lee, D.-H. (2015). Inferring Magnetospheric Heavy Ion Density using EMIC waves. *Journal of Geophysical Research Space Physics*, 120, doi:10.1002/2015JA021092.

Kim, E.-H., Johnson, J. R., & Lee, D.-H. (2019). Electron inertial effects on linearly polarized electromagnetic ion cyclotron waves at Earth's magnetosphere. *Journal of Geophysical Research: Space Physics*, 124 (4), 2643–2655. doi:https://doi.org/10.1029/2019JA026532

Kim, E.-H., Johnson, J. R., & Lee, K.-D. (2011). ULF wave absorption at Mercury. *Geophysical Research Letters*, 38, L16111, doi:10.1029/2011GL048621

Kim, E.-H., Johnson, J. R., Valeo, E., & Phillips, C. K. (2015). Global modeling of ULF waves at Mercury. *Geophysical Research Letters*, 42, 5147–5154, doi:10.1002/2015GL064531.

Kim, E.-H., & Lee, D.-H. (2005). Simulation study of electron and proton whistlers in the ionosphere. *Journal of the Korean Physical Society*, 46, 541–545.

Klaasen, K. P. (1976). Mercury's rotation axis and period. Icarus, 28 (4), 469-478. doi: https://doi.org/10.1016/0019-1035(76)90120-2

Klimushkin, D. Y., Mager, P. N., & Glassmeier, K.-H. (2006). Axisymmetric Alfvén resonances in a multi-component plasma at finite ion gyrofrequency. *Ann Geophys*, 24 , 1077–1084.

Lee, D.-H. & Lysak, R. L. (1989) Magnetospheric ULF Wave Coupling in the Dipole Model: The Impulsive Excitation, *Journal of Geophysical Research*, 94, 17097-17103, https://doi.org/10.1029/JA094iA12p17097

Lee, D.-H., Johnson, J. R., Kim, K., & Kim, K.-S. (2008). Effects of heavy ions on ULF wave resonances near the equatorial region. *Journal of Geophysical Research*, 113 , A11212, doi:10.1029/2008JA 013088.

Lee, D.-H., & Takahashi, K. (2006). MHD eigenmodes in the inner magnetosphere, in magnetospheric ULF waves: Synthesis and new directions (K. Takahashi, P. J. Chi, R. E. Denton, & R. L. Lysak, Eds.). American Geophysical Union, Washington, D. C. (doi: 10.1029/169GM07)

Lee, J. H., Blum, L. W., & Chen, L. (2021). On the impacts of ions of ionospheric origin and their composition on magnetospheric EMIC waves. *Frontiers in Astronomy and Space Sciences*, 8, 122. doi: 10.3389/fspas.2021.719715

Mikhailova, O. S., Mager, P. N., & Klimushkin, D. Y. (2019). Two modes of ion-ion hybrid waves in magnetospheric plasma. *Plasma Physics and Controlled Fusion*, 62 (2), 025026. doi: 10.1088/1361-6587/ab5b32

Min, K., Lee, J., Keika, K., & Li, W. (2012). Global distribution of EMIC waves derived from THEMIS observations. *Journal of Geophysical Research*, 117, A05219, doi:10.1029/2012JA017515.

Noh, S., Kim, H., Lessard, M., Engebretson, M., Pilipenko, V., Kim, E.-H., . . . Salzano, M. (2022). Statistical study of EMIC wave propagation using space-ground conjugate observations. *Journal of Geophysical Research*, https://doi.org/10.1029/2022JA030262

Pakhotin, I. P., Mann, I. R., Sydorenko, D., & Rankin, R. (2022). Novel EMIC wave propagation pathway through Buchsbaum resonance and interhemispheric wave interference: Swarm observations and modeling. *Geophysical Research Letters*, 49, e2022GL098249. https://doi.org/10.1029/2022GL098249

Park, K. S., Ogino, T., & Kim, Y. H. (2010). Effects of the dipole tilt and northward and duskward IMF on dayside magnetic reconnection in a global MHD simulation. *Journal of Geophysical Research: Space Physics*, 115 (A2). doi: https://doi.org/10.1029/2009JA014212

Philpott, L. C., Johnson, C. L., Winslow, R. M., Anderson, B. J., Korth, H., Purucker, M. E., & Solomon, S. C. (2014). Constraints on the secular variation of Mercury's magnetic field from the combined analysis of Messenger and Mariner 10 data. *Geophysical Research Letters*, 41 (19), 6627-6634. doi: https://doi.org/10.1002/2014GL061401

Rauch, J. L., & Roux, A. (1982). Ray tracing of ULF waves in a multicomponent magnetospheric plasma - Consequences for the generation mechanism of ion cyclotron waves. Journal of Geophysical Research, 87, 8191–8198.

Saikin, A. A., Zhang, J.-C., Allen, R. C., Smith, C. W., Kistler, L. M., Spence, H. E., . . . Jordanova, V. K. (2015). The occurrence and wave properties of H^+-, He^+-, and O^+-band EMIC waves observed by the Van Allen Probes. *Journal of Geophysical Research*, 120, doi:10.1002/2015JA021358.

Sakaguchi, K., Kasahara, Y., Shoji, M., Omura, Y., Miyoshi, Y., Nagatsuma, T., . . .Matsuoka, A. (2013). Akebono observations of EMIC waves in the slot region of the radiation belts. *Geophysical Research Letters*, 40, 5587–5591. doi:10.1002/2013GL058258

Shiraiwa, S., Wright, J. C., Bonoli, P. T., Kolev, T., & Stowell, M. (2017). RF wave simulation for cold edge plasmas using the MFEM library. *European physical journal web of conferences,* 157, 03048). doi:10.1051/epjconf/201715703048

Smith, R. L., & Brice, N. (1964). Propagation in Multicomponent Plasmas. *Journal of Geophysical Research*, 69, 5029–5040. doi: 10.1029/JZ069i023p05029

Usanova, M. E. (2021). Energy exchange between electromagnetic ion cyclotron (EMIC) waves and thermal plasma: From theory to observations. *Frontiers in Astronomy and Space Sciences*, 8, 150. doi: 10.3389/fspas.2021.744344

Wang, X. Y., Huang, S. Y., Allen, R. C., Fu, H. S., Deng, X. H., Zhou,

M., . . . Torbert, R. B. (2017). The occurrence and wave properties of EMIC waves observed by the Magnetospheric Multiscale (MMS) mission. *Journal of Geophysical Research: Space Physics*, 122 (8), 8228–8240. doi: https://doi.org/10.1002/2017JA024237

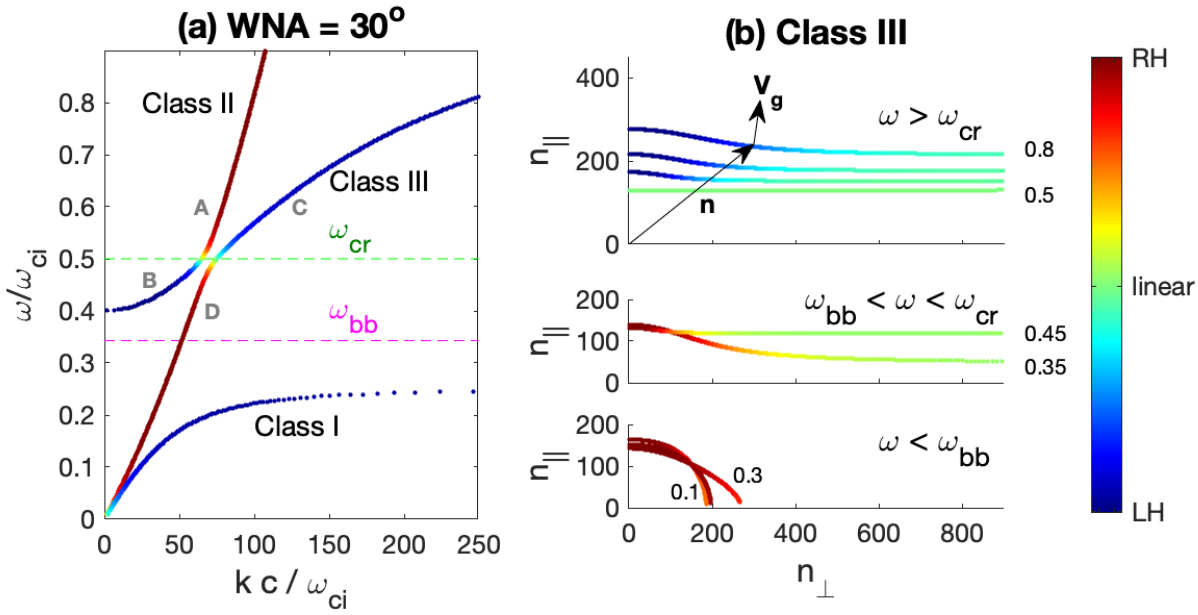

Figure 1. (a) Dispersion relation of ULF waves in the presence of 20 % He^+ ions. Horizontal green and magenta lines indicate the crossover ($_{cr} = 0.5\ _{ci}$) and Buchsbaum resonance ($_{bb} = 0.34\ _{ci}$) frequencies. Here, A, B, C, and D represent class II RHP, class II LHP, class III LHP, and class III RHP, respectively. (b) Refractive index surface of class III waves. Upper to bottom panels are for $_{cr}$ (/ $_{ci}$ = 0.5, 0.6, 0.7, and 0.8), $_{bb} <$ $<$ $_{cr}$ (/ $_{ci}$ = 0.35, and 0.45), and $<$ $_{bb}$ (/ $_{ci}$ = 0.1, 0.2, and 0.3), respectively. Arrows in the upper panel show the refractive index (n) and group velocity (V_g) directions. The color bar denotes a wave ellipticity. The plus (red) and minus (blue) signs are RHP and LHP.

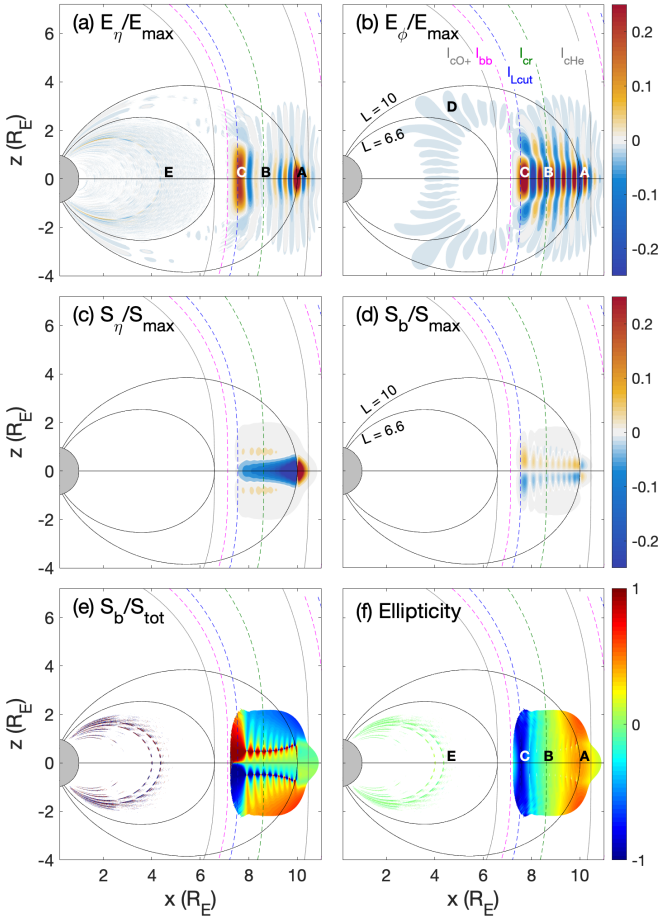

Figure 2. Wave solutions of lower latitude compressional wave source for 10% He^+ and 5% O^+ plasma. (a-b) Normalized electric field (E) to the maximum electric field amplitude ($Emax$), (c-d) Normalized Poynting flux (S) to the maximum of Poynting flux (S_{max}), (e) Normalized Poynting flux to the local total Poynting flux in each location (S_{tot}), and (f) wave ellipticity. Here, , , and b denote the orthogonal component the across the field line, azimuthal, and field-aligned directions, respectively. For the ellipticity, the plus and minus signs are RHP and LHP circularly polarization. Horizontal black line is magnetic equator and Grey, magenta, blue, green lines are where wave frequency matches to He^+ and O^+ gyro- ($l_{\rm cHe}$, $l_{\rm cO}$), Buchsbaum resonance ($l_{\rm bb}$), LHP wave cutoff ($l_{\rm Lcut}$), crossover ($l_{\rm cr}$) frequencies, respectively.

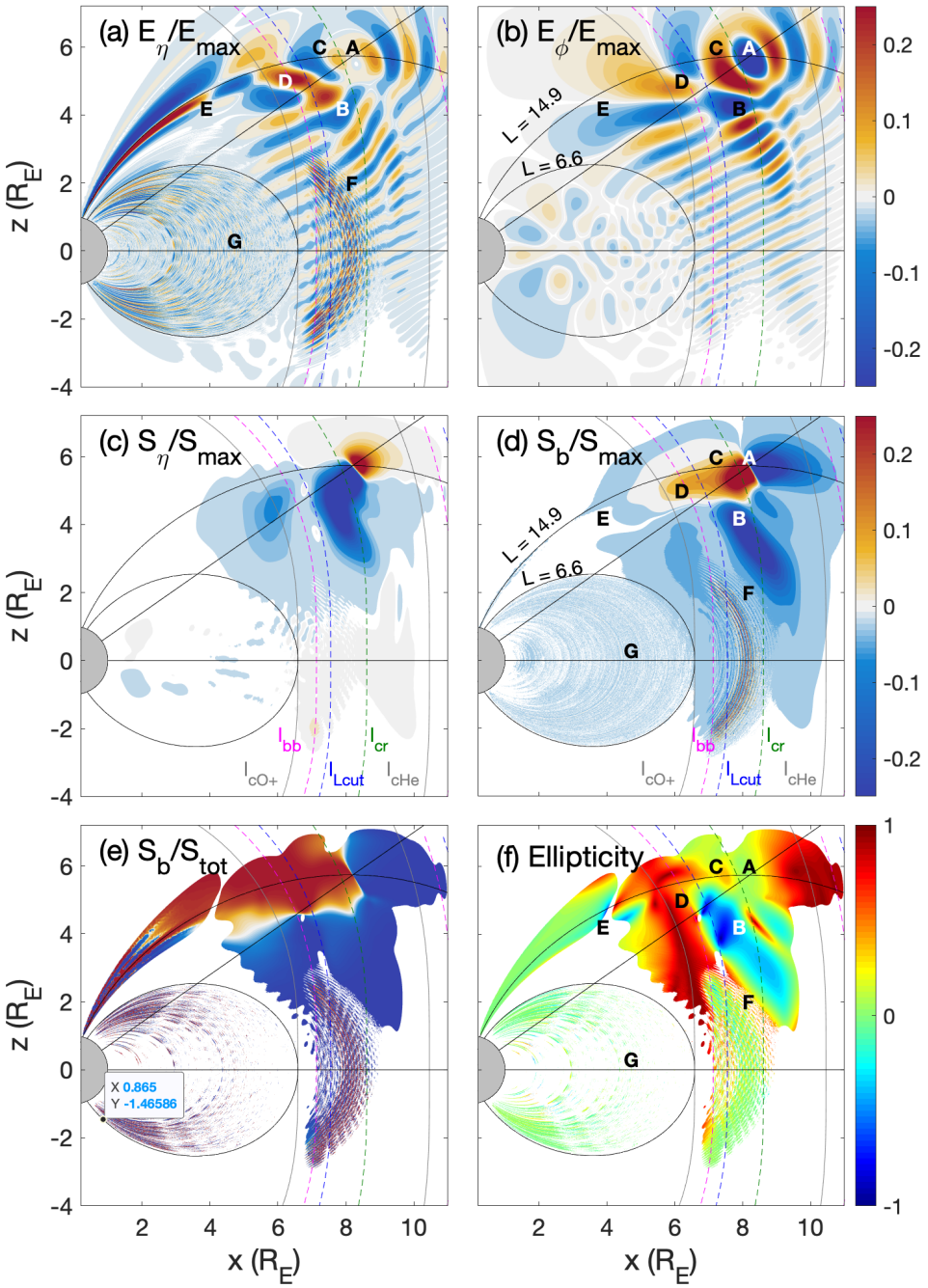

Figure 3. The same as Figure 2 for off magnetic equator compressional wave. The horizontal and diagonal black lines are the magnetic equator and the ecliptic

plane, respectively. In this case, the source located at the ecliptic plane at $L = 14.9$ where $R = 10R_E$.